

Article

Au Nanoparticles Decorated Graphene-Based Hybrid Nanocomposite for As(III) Electroanalytical Detection

Valentina Pifferi ^{1,*}, Anna Testolin ¹, Chiara Ingrosso ^{2,*}, Maria Lucia Curri ^{2,3}, Iliaria Palchetti ⁴ 
and Luigi Falcicola ¹ 

¹ Department of Chemistry, Università degli Studi di Milano, Via Golgi 19, 20133 Milano, Italy; anna.testolin92@gmail.com (A.T.); luigi.falcicola@unimi.it (L.F.)

² CNR-IPCF, Istituto per i Processi Chimico-Fisici, S.S. Bari, c/o Dip. Chimica Via Orabona 4, 70126 Bari, Italy; marialucia.curri@uniba.it

³ Department of Chemistry, Università degli Studi di Bari, Via Orabona 4, 70126 Bari, Italy

⁴ Department of Chemistry Ugo Schiff, Università degli Studi di Firenze, Via della Lastruccia 3-13, 50019 Sesto Fiorentino, Italy; ilaria.palchetti@unifi.it

* Correspondence: valentina.pifferi@unimi.it (V.P.); c.ingrosso@ba.ipcf.cnr.it (C.I.)

Abstract: Electrochemical sensors integrating hybrid nanostructured platforms are a promising alternative to conventional detection techniques for addressing highly relevant challenges of heavy metal determination in the environment. Hybrid nanocomposites based on graphene derivatives and inorganic nanoparticles (NPs) are ideal candidates as active materials for detecting heavy metals, as they merge the relevant physico-chemical properties of both the components, finally leading to a rapid and sensitive current response. In this work, a hybrid nanocomposite formed of reduced graphene oxide (RGO) sheets, surface functionalized by π - π interactions with 1-pyrene carboxylic acid (PCA), and decorated *in situ* by Au NPs, was synthesized by using a colloidal route. The hybrid nanocomposite was characterized by cyclic voltammetry and electrochemical impedance spectroscopy with respect to the corresponding single components, both bare and deposited as a layer-by-layer junction onto the electrode. The results demonstrated the high electrochemical activity of the hybrid nanocomposite with respect to the single components, highlighting the crucial role of the nanostructured surface morphology of the electrode and the PCA coupling agent at the NPs-RGO interphase in enhancing the nanocomposite electroactivity. Finally, the Au NP-decorated PCA-RGO sheets were tested by anodic stripping voltammetry of As(III) ion—a particularly relevant analyte among heavy metal ions—in order to assess the sensing ability of the nanocomposite material with respect to its single components. The nanocomposite has been found to present a sensitivity higher than that characterizing the bare components, with LODs complying with the directives established by the U.S. EPA and in line with those reported for state-of-the-art electrochemical sensors based on other Au-graphene nanocomposites.

Keywords: reduced graphene oxide; Au nanoparticles; pyrene linker; hybrid nanocomposite; As(III) detection; electrochemical sensor



Citation: Pifferi, V.; Testolin, A.; Ingrosso, C.; Curri, M.L.; Palchetti, I.; Falcicola, L. Au Nanoparticles Decorated Graphene-Based Hybrid Nanocomposite for As(III) Electroanalytical Detection. *Chemosensors* **2022**, *10*, 67. <https://doi.org/10.3390/chemosensors10020067>

Academic Editor: Gabriella Leo

Received: 29 December 2021

Accepted: 5 February 2022

Published: 8 February 2022

Publisher's Note: MDPI stays neutral with regard to jurisdictional claims in published maps and institutional affiliations.



Copyright: © 2022 by the authors. Licensee MDPI, Basel, Switzerland. This article is an open access article distributed under the terms and conditions of the Creative Commons Attribution (CC BY) license (<https://creativecommons.org/licenses/by/4.0/>).

1. Introduction

Hybrid nanocomposites based on inorganic nanoparticles (NPs) and graphene derivatives combine the unique size- and shape-dependent properties of inorganic matter at nanoscale [1] with the outstanding properties of graphene derivatives, allowing access to novel interesting multifunctionalities for diverse technology purposes [2,3].

In particular, a novel class of multifunctional hybrid nanocomposites can be ingeniously designed by exploiting the high chemical reactivity of graphene. Graphene can be functionalized with aromatic ligands anchoring the basal plane by π - π interactions without detrimentally affecting its structural properties, and can concomitantly coordinate inorganic NPs with different chemical compositions (metal, II-VI chalcogenide semiconductor, oxide).

Hence, a plethora of interesting functionalities are possible [4], which can be integrated in sensors for the detection of hazardous compounds.

Arsenic(III) (As(III)) is a highly toxic heavy metal ion (HMI) responsible for contamination of surface and groundwater, deriving both from natural and anthropogenic sources [5]. It is hazardous to the environment and human health, even at trace levels, as it accumulates in living organisms and disturbs the biochemical activity of enzymes, leading to disorders of nervous, immune, reproductive and gastrointestinal systems [6]. The biological damage caused by As(III) has been found to be 20–30 times more than that of As(V). Furthermore, removal of As(III) from natural water is more difficult than As(V) [7]. In view of these adverse effects, WHO (World Health Organization) and U.S.-EPA (United States Environmental Protection Agency) have recommended that the permissible level of As in drinking water should be as low as 10 ppb [8], leading to the development of methods to detect As(III) as a priority to fulfill such directives.

Several analytical techniques (i.e., AAS [9], ICP-MS [10] and ICP-OES [11]) have been used to detect As(III) in complex matrices with very low limits of detection (LODs) while also allowing simultaneous determination of diverse elements. However, though suitable for quantitative analysis, they often require an analyte pre-concentration step in the matrix, need to be coupled with other chromatographic techniques to perform ion speciation, are expensive, time consuming, and sometimes require multisampling with difficult analytical procedures that must be performed by trained personnel. Optical techniques can be used for As(III) detection in water, but they are costly and require complex equipment, high precision and high-power operations [12].

Electrochemical methods overcome these drawbacks, as they are more cost-effective, user-friendly, reliable, and allow the use of miniaturized devices which can be easily modified onto the surface with diverse multifunctionalities [13]. The compact and portable instrumentation facilitates online and on-site measurements for continuous monitoring [14]. Such integrated processes ensure a novel risk assessment-based approach to evaluate the environmental status, including chemical quality, morphological conditions, and ecological safety (regulated in Europe by the Water Framework Directive (WFD) 2000).

This class of methods, however, may suffer from lower sensitivity and LODs higher than those characterizing other analytical techniques, and hence, may require highly specific biosensing approaches. Immunosensors have been reported to use nanostructured platforms in the electroanalytical determination of As(III), particularly with anodic stripping voltammetry (ASV), by exploiting the excellent redox electrocatalytic activity of Au NPs and high rate of electron transfer kinetics at the electrode/electrolyte interface [15]. Screen-printed electrodes (SPCEs), modified by Au NPs coated by L-cysteine conjugated to reduced lipoic acid, have been used for the detection of As(III) in ground water by square-wave anodic stripping voltammetry (SWV-ASV) [16].

On the other hand, the high conductivity and high electrocatalytic activity typical of graphene derivatives [17] have been used for the detection of As(III) in broiler meat by cyclic voltammetry, with a LOD of 3 ppb by modifying glassy carbon electrodes (GCEs) with the GO-Co/2-(4,5-diphenyl-1H-imidazol-2-yl)phenol (DIP) composite [18].

Hybrid nanocomposites formed of reduced graphene oxide (RGO), surface coated by electrodeposited Au NPs, have been used for detecting As(III) in water and soil samples [19] with high sensitivity and ease of application, thanks to the merging of the intrinsic functionalities of both components. In this work, nanoplateforms formed of carbon screen-printed electrodes (C-SPEs) surface modified by a hybrid nanocomposite formed of reduced graphene oxide (RGO), functionalized with 1-pyrene carboxylic acid (PCA), then decorated by a dense and uniform layer of Au NPs that were synthesized by an *in situ* approach [4], were investigated by cyclic voltammetry (CV) and electrochemical impedance spectroscopy (EIS). These have been tested for the detection of As(III) in water, and their properties have been compared with respect to C-SPEs modified by bare PCA-RGO and Au NPs alone, and by their layer-by-layer PCA-RGO@Au NPs junction. The results have shown that the hybrid modified electrodes presented enhanced conductivity and electroactivity compared

to its single components and the layer-by-layer PCA-RGO@Au NPs junction. They also have demonstrated a higher sensitivity in the detection of As(III), with a LOD of the same order of magnitude of the limits imposed by the directives and laws on the maximum amount of As in public water supplies (i.e., 10 ppb as established by USA EPA) and of those reported in literature [16,18–20]. These results have been ascribed to the crucial role of the PCA linker behaving as a coupling agent at the RGO-Au NPs interphase, effectively merging the unique properties of the hybrid components and resulting in enhanced electrochemical activity.

2. Materials and Methods

2.1. Chemicals

Commercial reduced graphene oxide (RGO) (1.6 nm flakes) was purchased from Graphene Supermarket. Additionally, 1-Pyrene Carboxylic Acid (PCA, 97%), n-methyl-2-pyrrolidone (NMP, 99%), tetraoctylammonium bromide (TOAB, 99%), hydrogen tetrachloroaurate(III) hydrate ($\text{HAuCl}_4 \cdot 3\text{H}_2\text{O}$, 99.999%), 3,4-dimethylbenzenethiol (DMBT, 98%), sodium borohydride (NaBH_4 , 99.99%), As_2O_3 , toluene, and methanol were purchased from Sigma Aldrich.

2.2. Exfoliation and Functionalization of RGO with PCA

Commercial RGO powder was exfoliated and functionalized with 1-Pyrenecarboxylic acid (PCA) by sonicating in an ice-cooled water bath, a 1:17 *w/w* mixture of RGO and PCA in n-methyl-2-pyrrolidone (NMP). The excess of PCA was removed by cycles of centrifugation and redispersion in methanol [4]. Finally, the purified PCA-RGO powder was dispersed in NMP, obtaining a final concentration of 3 mg mL⁻¹.

2.3. Synthesis of PCA-RGO/Au NPs Hybrid Nanocomposite

For the preparation of the PCA-RGO/Au NPs hybrid nanocomposite, the two-phase method of M. Brust et al. [21], used for the synthesis of thiol-coated Au NPs, was followed with minor modifications. Briefly, 15 mg of PCA-RGO were dispersed in NMP and then added to a solution prepared by mixing 2.3744 g of TOAB in 35 cm³ of toluene, left to stir 30 min. Then, 0.354 g of $\text{HAuCl}_4 \cdot 3\text{H}_2\text{O}$, dispersed in 15 cm³ of Milli-Q water, were added and left to stir 30 min. After TOAB-assisted transfer of the Au precursor from the water to the toluene phase, water was removed from the reaction flask, 60 μL of DMBT were added and the solution was left to stir 1 h. The thiol allowed the slow reduction of Au(III) to Au(I) which was then reduced to Au(0) by addition of 0.378 g of NaBH_4 in 25 cm³ of Milli-Q water, and behaved as a coordinating agent for the formed Au NPs. The whole process was performed at room temperature.

The PCA-RGO/Au NPs dispersions were purified with methanol by cycles of precipitation by centrifugation and redissolution in solvent. In a final step, a precipitation procedure was performed by addition of methanol and centrifugation, in order to separate the PCA-RGO/Au NPs hybrid nanocomposite from the DMBT-coated Au NPs homonucleated in the supernatant of the reaction solution [4]. The isolated pellet containing the hybrid nanocomposite was finally redispersed in toluene for spectroscopy, morphology, electrical and electrochemical characterizations.

2.4. Synthesis of DMBT-Coated Au NPs

The synthesis of the DMBT-capped Au NPs was also performed under the same conditions of the procedure followed for obtaining the PCA-RGO/Au NP hybrid nanocomposite, except for the addition of PCA-RGO. Thus, DMBT-coated Au NPs in toluene, spherical in shape and 2–3 nm in size, were synthesized.

2.5. Characterization Techniques

UV-Vis-NIR absorption spectra of the PCA-RGO/Au NP hybrid nanocomposite dispersed in toluene were recorded using a Cary Varian 5000 spectrophotometer.

TEM analyses were performed using a Jeol Jem-1011 microscope operating at 100 kV, equipped with a high-contrast objective lens and a W filament as an electron source, having an ultimate point resolution of 0.34 nm. Images were acquired by a Quemesa Olympus CCD 11 MP Camera. Samples were prepared by dipping a 300-mesh amorphous carbon-coated Cu grid in toluene solutions of the PCA-RGO/Au NPs hybrid pellet and leaving the solvent to evaporate. Size statistical analysis of the NPs average size and size distribution was performed using the ImageJ analysis program.

Raman spectra were recorded using a LabRAM HR Horiba-Jobin Yvon spectrometer with a 532 nm continuous excitation laser source. Measurements were carried out under ambient conditions at low laser power (1 mW) to avoid laser-induced damage of the sample. Raman signal from a silicon wafer at 520 cm^{-1} was used to calibrate the spectrometer, and accuracy of the spectral measurement was estimated to be 1 cm^{-1} .

2.6. Preparation of the Electrodes Modified by PCA-RGO/Au NPs Hybrid Pellet, PCA-RGO and DMBT-Au NPs

Carbon screen-printed electrodes (C-SPEs) (purchased from Metrohm DropSens) were modified by casting: (i) $1.8\ \mu\text{L}$ of a toluene solution of the PCA-RGO/Au NPs hybrid nanocomposite, isolated by centrifugation from a sample synthesized starting from 3 mg mL^{-1} PCA-RGO and $2 \times 10^{-4}\text{ M}$ DMBT-coated Au NPs; (ii) $1.8\ \mu\text{L}$ of a toluene solution 3 mg mL^{-1} in PCA-RGO; and (iii) $1.8\ \mu\text{L}$ of a toluene solution $2 \times 10^{-4}\text{ M}$ in DMBT-coated Au NPs. Layer-by-layer films of PCA-RGO and Au NPs were prepared onto C-SPEs by casting $1.8\ \mu\text{L}$ of a 3 mg mL^{-1} PCA-RGO solution and then $1.8\ \mu\text{L}$ of a $2 \times 10^{-4}\text{ M}$ DMBT-Au NPs solution, both in toluene. This layer-by-layer sample was indicated herein as PCA-RGO@Au NPs.

2.7. Electrochemical Characterizations

The modified C-SPEs were electrochemically characterized by cyclic voltammetry (CV) and electrochemical impedance spectroscopy (EIS) using a PGStat30 potentiostat/galvanostat equipped with the NOVA 2.1 Software (Metrohm AutoLab, Utrecht, The Netherlands). The experiments were carried out in a conventional three-electrode cell using the modified C-SPEs, saturated calomel electrode (SCE), and a Platinum wire, as working (WE), reference (RE), and counter (CE) electrodes, respectively. Additionally, 0.1 M solutions of KCl, NaClO_4 , and PBS (Phosphate Buffer, pH 7.4) were used as supporting electrolytes and $\text{K}_4[\text{Fe}(\text{CN})_6]$ was selected as a molecular redox probe. The current density values were normalized with respect to the geometric area of the electrodes, 0.126 cm^2 . EIS measurements were carried out at -0.1 V , $+0.1\text{ V}$, and $+0.25\text{ V}$ (SCE) in the frequency range of 0.01 and 100,000 Hz, in the background and in the presence of the redox probe, in the above-mentioned electrolytes.

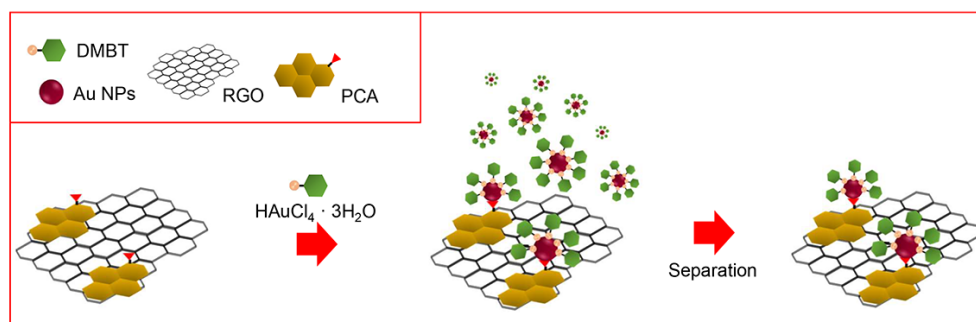
2.8. Electroanalytical Applications

As_2O_3 was dissolved in a 0.1 M NaOH aqueous solution. The μ -AutoLab III potentiostat/galvanostat, equipped with the NOVA 2.1 Software (Metrohm AutoLab, Utrecht, The Netherlands), was used for voltammograms registration. For As detection, anodic stripping voltammetry (ASV) was used as the electroanalytical technique. This comprised a preliminary accumulation step at the cathodic potential of $+0.8\text{ V}$ (SCE) for 60 s, in order to reduce As(III) or As(V) ions in solution to As(0), followed by a linear sweep in the anodic scan direction, from -0.4 V to $+0.8\text{ V}$ (SCE) at the scan rate of 0.1 V s^{-1} . The analyses were performed in 0.1 M PBS at pH 7.4, which this electrolyte preferred over acidic conditions [19], after degassing the electrolyte solution with N_2 for 15 min, and after As_2O_3 additions.

3. Results and Discussion

3.1. Synthesis and Characterization of the PCA-RGO/AuNPs Hybrid Nanocomposite

The PCA-RGO/Au NP hybrid nanocomposite has been synthesized by following the *in situ* approach reported in [4], relying on a modification of the two-step chemical route of M. Brust et al. [21]. In this approach, the $\text{HAuCl}_4 \cdot 3\text{H}_2\text{O}$ precursor is reduced in the presence of the DMBT thiol and of NaBH_4 to Au NPs, which heteronucleate and grow onto the oxygen-based functionalities of the PCA-RGO basal plane (Scheme 1). DMBT slowly reduces Au(III) to Au(I), which is then reduced by NaBH_4 to Au NPs, controls NPs morphology and size dispersion behaving as a coordinating ligand, promotes further NPs anchoring onto the RGO basal plane by π - π interactions, and stabilizes the NPs in organic solvents [4].



Scheme 1. Sketch of the *in situ* synthesis of the DMBT-capped Au NPs onto the PCA-RGO basal plane.

In the synthesis of the nanocomposite, concomitant homonucleation of the Au NPs in the reaction solution has been observed (Scheme 1), and thus, the hybrid nanostructures are separated by the homonucleated Au NPs by a post-synthetic precipitation procedure. Such a separation procedure relies on a slow addition of methanol, as an antisolvent for the synthesized PCA-RGO/Au NPs, thus inducing gradual and selective flocculation of the larger PCA-RGO/Au NPs, [4] that can be thus isolated and separated, by centrifugation, as a precipitate pellet, from the supernatant containing the smaller DMBT-capped Au NPs.

The TEM micrograph of the PCA-RGO complex has shown almost electron transparent sheet-like structure, accountable for exfoliated RGO sheets [4], with high contrast areas reasonably due to folded edges and wrinkles, due to mechanical lattice deformations of the basal plane (Figure 1A) [22]. On the other hand, the PCA-RGO/Au NPs hybrid nanocomposite presents sheets-like structures uniformly and densely coated by spherical and high contrast nanostructures, 2–3 nm in size, reasonably ascribed to the formed Au NPs (Figure 1B,C).

The Raman spectra of PCA-RGO and PCA-RGO/Au NPs (Figure 1D) has presented the typical D and G Raman modes of graphitic materials at ca. 1340 cm^{-1} and 1590 cm^{-1} , respectively [23], assessing retention of the RGO structure upon *in situ* synthesis of the Au NPs. In the Raman spectrum of the hybrid nanocomposite, a broad background signal has been observed, reasonably originating from the PCA photoluminescence [24], along with an intensity ratio between the D and G peaks lower than PCA-RGO, indicating a reduction of the RGO defects [4,5], resulting from the treatment with NaBH_4 and catalyzed by the immobilized Au NPs [25].

The UV-Vis-NIR absorption spectra of PCA-RGO/Au NPs have shown the characteristic localized surface plasmon resonance (LSPR) band of spherical and low nm in size Au NPs, at 519 nm. This originates from collective excitation of free conduction band electrons and its position is affected by the NPs local environment (i.e., solvent, capping ligand, supporting substrate and presence of adjacent NPs) [26] along with the absorption features in the UV spectral region, ascribed to π - π^* transitions of the pyrene linker, confirming its anchoring onto the RGO basal plane [4,27] (Figure 1E).

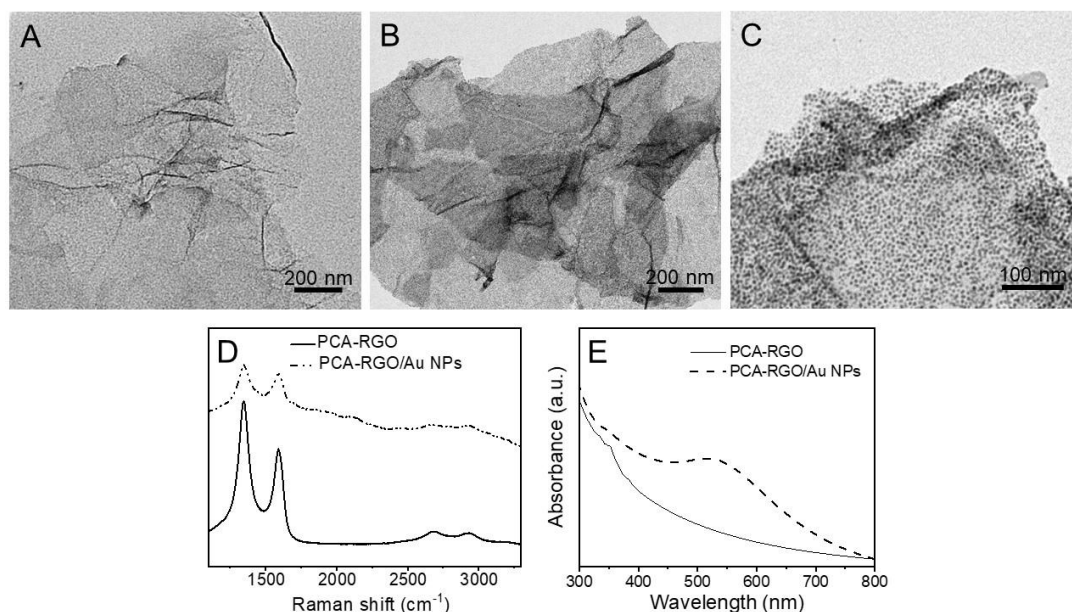
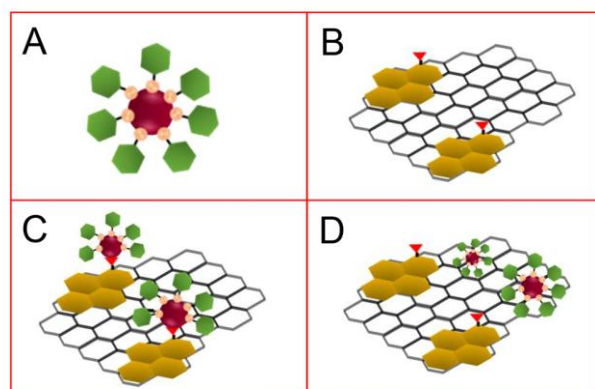


Figure 1. TEM micrographs of (A) PCA-RGO and (B,C) PCA-RGO/Au NPs (40 Kx and 60 Kx, respectively). (D) Raman and (E) UV-Vis-NIR spectra of 0.15 mg mL^{-1} PCA-RGO and 0.15 mg mL^{-1} PCA-RGO/Au NPs, $7 \cdot 10^{-3} \text{ M}$ in Au NPs and 2 mg mL^{-1} in PCA-RGO in toluene.

3.2. Electrochemical Characterization of the PCA-RGO/Au NPs Hybrid Nanocomposite

C-SPEs have been modified by drop casting the DMBT-coated Au NPs, PCA-RGO, PCA-RGO/Au NPs and the layer-by-layer PCA-RGO@Au NPs samples (Scheme 2). The electrochemical and electrical properties have been investigated by cyclic voltammetry (CV) and electrochemical impedance spectroscopy (EIS).



Scheme 2. Sketch of the materials used to modify the C-SPEs: (A) DMBT-coated Au NPs, (B) PCA-capped RGO, (C) PCA-RGO/Au NPs hybrid nanocomposite and (D) PCA-RGO@Au NPs layer-by-layer junctions.

Figure 2 reports the CVs of the modified C-SPEs, registered both in absence (Figure 2A) and presence of the inner-sphere redox probe $\text{K}_4[\text{Fe}(\text{CN})_6]$ [28], added to KCl, NaClO_4 , and PBS supporting electrolytes (Figure 2B–D), respectively.

$\text{K}_4[\text{Fe}(\text{CN})_6]$ has been selected as an inner-sphere probe to study the electron transfer and structural properties of the modified electrodes, as its electrochemical behavior has been found more sensitive to the chemistry (oxygen containing functionalities, impurities, and adsorption sites) and structure of the electrode material surface, rather than its electronic density of states (DOS) [29].

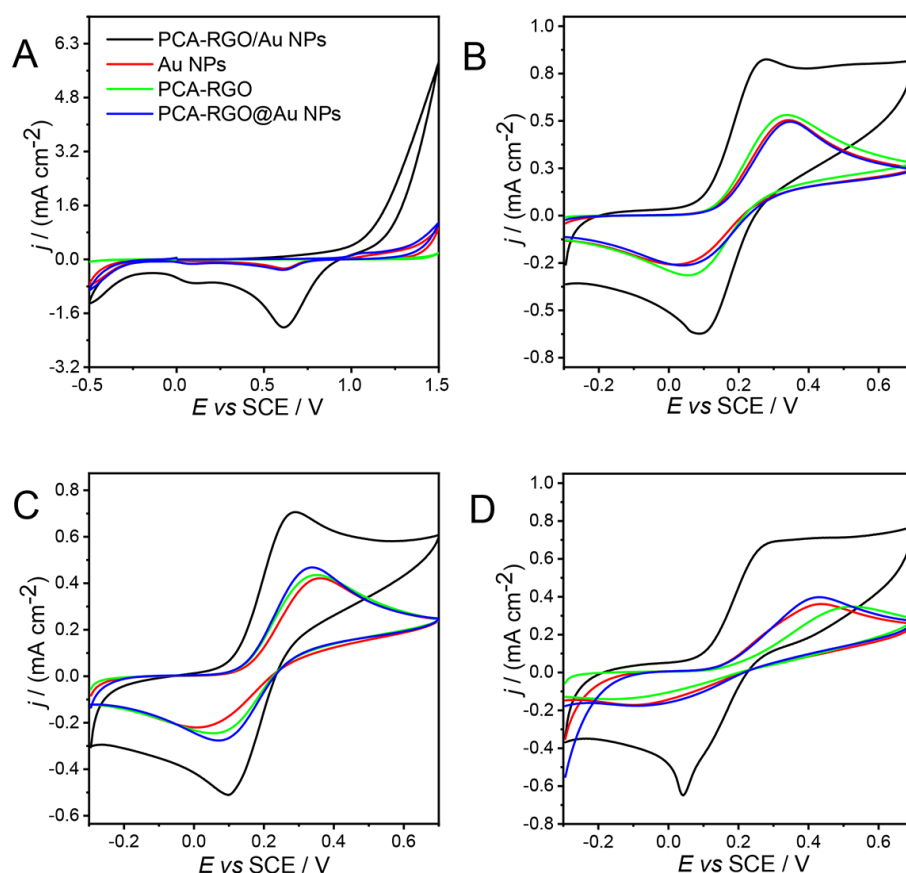


Figure 2. CV curves of C-SPEs modified by PCA-RGO/Au NPs, PCA-RGO, DMBT-Au NPs, and PCA-RGO@Au NPs at 100 mV s^{-1} , in 0.1 M (A) NaClO_4 , 0.1 M (B) NaClO_4 , (C) KCl , and (D) PBS aqueous solutions, with the addition of $3 \text{ mM K}_4[\text{Fe}(\text{CN})_6]$ (B–D).

The cyclic voltammograms of the C-SPEs modified by PCA-RGO/Au NPs, DMBT-Au NPs and PCA-RGO@Au NPs have shown, in NaClO_4 , two cathodic peaks at ca. 0.1 V and 0.6 V (SCE) (Figure 2A), the latter being the classical peak due to the dissolution of the gold oxide layer formed in the anodic region [27].

It has been noted that, in spite of the lower amount of Au NPs in the PCA-RGO/Au NPs sample, it has presented the highest current density. This has been ascribed to the fact that, despite starting from the same amount of Au precursor, part of Au homonucleates in the reaction solution instead of heteronucleating on PCA-RGO. Thus, the highest current signal of the PCA-RGO/Au NPs C-SPEs has been ascribed to the increase of the electrode conductivity and to the enhancement of the heterogeneous electron transfer kinetics at the electrode/electrolyte interface. This has been also due to the presence of the PCA linker anchored onto the RGO basal plane by π - π interactions, which acts as an electron coupling agent between the Au NPs and RGO [4,27,30]. In addition, Figure 2B–D have shown that, in each investigated electrolyte, the PCA-RGO/Au NPs C-SPEs exhibit an electrochemical behavior in presence of the inner sphere redox probe, that differs from that of the other electrodes. These have shown the highest current density—which, again, could be accounted for by the high electrochemical activity of the hybrid electrodes—and high electrocatalytic activity, as evidenced by the shift of the oxidation and reduction peaks towards lowest potentials (Figure 2B–D, Table 1). Such an evidence addresses a more energetically favored red/ox process and more reversible electrochemical behavior, due to an increased electron transfer rate. This latter can be probably also related to a thin layer diffusion process.

Table 1. Anodic peak potential (E) and current density (j) of 3 mM $K_4[Fe(CN)_6]$ in $NaClO_4$, KCl and PBS electrolytes at the voltage scan rate of 100 mV s^{-1} and electrode geometric area of 0.126 cm^2 .

	$NaClO_4$			KCl		PBS	
	E/V	$j/(mA\text{ cm}^{-2})$	$\log(i)$ vs. $\log(v)$ Slope	E/V	$j/(mA\text{ cm}^{-2})$	E/V	$j/(mA\text{ cm}^{-2})$
PCA-RGO/Au NPs	0.28	0.750	(0.39 ± 0.01)	0.28	0.599	0.28	0.546
Au NPs	0.34	0.482	(0.47 ± 0.02)	0.35	0.355	0.43	0.300
PCA-RGO	0.33	0.496	(0.412 ± 0.005)	0.35	0.408	0.52	0.318
PCA-RGO@Au NPs	0.35	0.472	(0.47 ± 0.02)	0.33	0.402	0.42	0.309

Moreover, the CVs of panels B–D, except for those of the PCA-RGO/Au NPs C-SPEs, have presented a peak-shaped profile that has been explained by a semi-infinite diffusion mechanism of the redox probe toward the electrode, which, hence, behaves as a macroelectrode [31].

Panels B and D in Figure 2 have pointed out that the interaction of the inner-sphere redox probe with the PCA-RGO/Au NPs electrodes, both in $NaClO_4$ and in PBS, leads to step-shaped voltammograms [31]. These results have been explained by the sensitivity of the redox probe toward the electrocatalytic Au NPs, which behaves as independent electroactive spots onto the RGO platform, forming a microarray of electrodes and providing a convergent diffusion mechanism of the probe to the electrode [32], resulting in the observed sigmoidal CVs typical of a microelectrode [33,34].

In PBS, the current density of the PCA-RGO/Au NPs electrodes have been found lower than in KCl and $NaClO_4$, and the CV profile tends more toward a step-shaped signal. These findings can be reasonably accounted for by absorption phenomena of the phosphate ions onto the RGO basal plane, which are then stripped away in the following reduction [35], leaving more available sites for the reaction of the redox probe and leading to a rapid enhancement of the reductive current density.

Further supporting the indication that PCA-RGO does not contribute to the red/ox processes of the probe, irrespective of the nature of the supporting electrolyte, the most positive potential values of the anodic peak have been highlighted (Figure 2, Table 1), confirming that the oxidation of such an electrode is less energetically favored. Conversely, Au NPs and PCA-RGO@Au NPs have shown comparable anodic peak potentials (Figure 2, Table 1) indicating the involvement of Au NPs in catalyzing the red/ox processes of the probe.

Cyclic voltammetry has been performed at different voltage scan rates (v) in the $10\text{--}500\text{ mV s}^{-1}$ range in order to investigate in detail the reversibility of the red/ox process and the diffusional mechanism of the $K_4[Fe(CN)_6]$ probe at the electrodes.

The results collected for the $NaClO_4$ electrolyte solution are shown in Table 1. All the modified C-SPEs have presented a linear dependence of the current density with the square root of the scan rate, but the wave-shape profile and the variability of the peak-to-peak current with the voltage scan rate have assessed the quasi-reversible electrochemical behavior of the system [34]. As far as the slope of the $\log(j)$ vs. $\log(v)$ graph, in case of the Au NPs, this value has been found close to 0.5, which is the value expected for a semi-infinite diffusive mechanism of the red/ox probe towards the electrode [34]. The PCA-RGO@Au NPs modified C-SPEs have shown the same slope as the Au NPs, while the hybrid modified C-SPEs have the lowest values, as a confirmation of the occurrence of a different diffusion mechanism of the redox probe—specifically, the previously mentioned convergent diffusion [34].

Electrochemical impedance spectroscopy (EIS) of the C-SPEs modified by PCA-RGO/Au NPs, PCA-RGO, Au NPs and PCA-RGO@Au NPs, have been collected in $NaClO_4$, in presence of the $K_4[Fe(CN)_6]$ redox probe at $+0.25\text{ V}$ (SCE).

The Complex plane and Bode Phase plots are reported in Figure 3A,B. The corresponding theoretical equivalent circuits derived by using the Software ZView, are reported in Figure 3C.

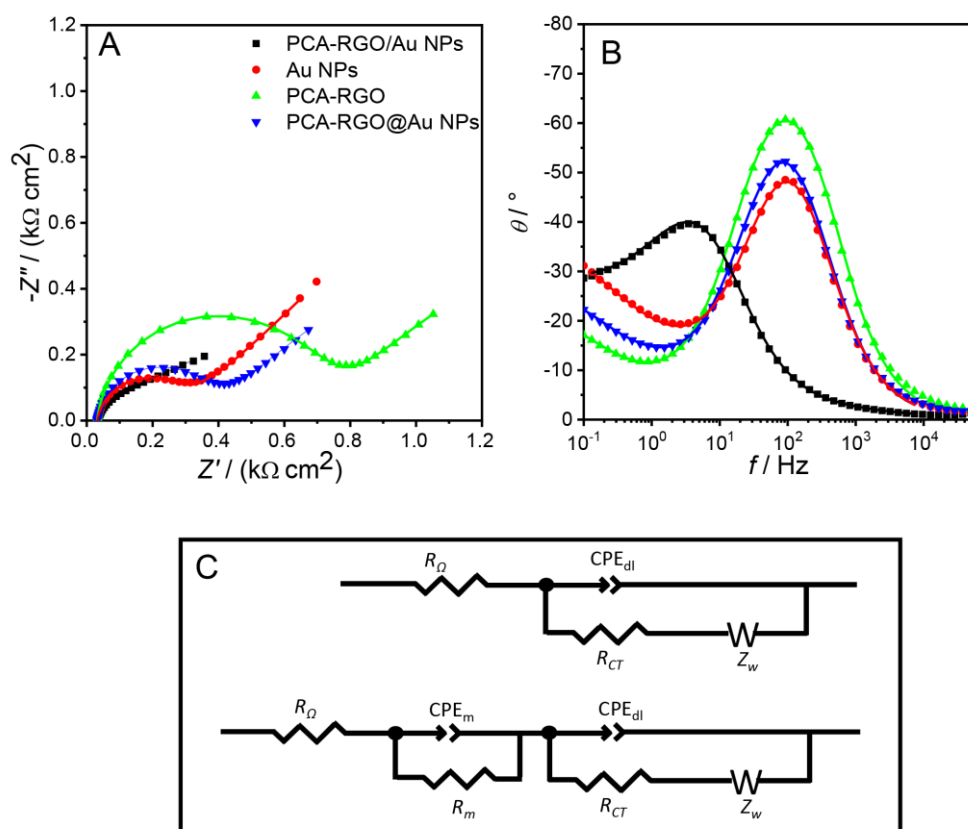


Figure 3. Complex plane (A) and Bode Phase (B) plots of the C-SPEs modified by PCA-RGO/Au NPs, Au NPs, PCA-RGO, and PCA-RGO@Au NPs in 0.1 M NaClO₄ added by 3 mM K₄[Fe(CN)₆] and recorded at +0.25 V (SCE). (C) Equivalent circuits derived from the EIS spectra of Au NPs, PCA-RGO and PCA-RGO@Au NPs (top panel) and of PCA-RGO/Au NPs (low panel) modified C-SPEs.

As noted, the theoretical equivalent circuit of the PCA-RGO, Au NPs, and PCA-RGO@Au NP-modified C-SPEs (Figure 3C, top panel) differs from those of the PCA-RGO/Au NPs electrodes (Figure 3C, low panel), assessing differences in the electrical properties.

In both the circuit models reported in Figure 3C, R_{Ω} is the resistance of the charge transfer at the electrode/electrolyte interphase. In the top panel, in series with R_{Ω} , there is the typical Randles circuit, which is composed of a constant phase element that mimics an ideal parallel plate capacitor (CPE_{dl})—taking into account the surface morphology of the electrode and the total impedance of the Faradaic reaction of the probe at the electrode surface. CPE_{dl} originated from the Debye layer, i.e., the layer of ions accumulates in proximity to the electrode for capacitive coupling, for compensating the charge accumulated at the hybrid electrode surface.

The capacitance values have been modeled as constant phase elements (CPEs) by the following equation:

$$CPE = [(Ci\omega)^{\alpha}]^{-1}$$

where C is the capacitance, i a complex number, ω the frequency, and α the parameter of deviation from the pure capacitance behavior.

The model has provided for $\alpha = 1$, a perfect and continuous working electrode which behaves as a pure capacitor. On the other hand, if $0.5 < \alpha < 1$, a nonideal capacitor behavior would be expected due to the non-homogenous porous electrode surface.

In the Randles circuit, in parallel with CPE_{dl} , there is R_{ct} , the resistance of the charge transfer between the probe and electrode surface, which has been estimated by the semicircle at the higher frequencies of Figure 3A.

The fitting of the EIS Bode-phase plots (Figure 3B) have provided an estimation of the values of resistance and capacitance of the equivalent circuits of Figure 3C, reported in Table 2.

Table 2. Estimated values of cell resistance (R_{Ω}), double layer capacitance (CPE_{dl}), charge transfer resistance (R_{ct}), Warburg resistance (Z_w), material capacitance (CPE_m), and material resistance (R_m).

Electrode	R_{Ω}/Ω cm^2	$CPE_m/(mF$ $cm^{-2}s^{\alpha-1})$	α_m	$R_m/$ (Ωcm^2)	$CPE_{dl}/(\mu F$ $cm^{-2}s^{\alpha-1})$	α_{dl}	$R_{ct}/(\Omega cm^2)$	$Z_w/(\Omega cm^2)$	α_w	τ_w (s)
PCA-RGO/Au NPs	31.16	2.78	0.55	3.48	684.16	0.86	126	2.55	0.38	422
Au NPs	32.71	-	-	-	29.85	0.92	260	3.04	0.50	42
PCA-RGO	31.55	-	-	-	18.46	0.93	676	1.50	0.47	18
PCA-RGO@Au NPs	31.85	-	-	-	29.09	0.92	334	1.42	0.46	24

The Table shows that the PCA-RGO/Au NPs C-SPEs present the highest CPE_{dl} (likely due to the increase of the carrier density of RGO provided by the PCA-induced electron coupling with the Au NPs). They also have the lowest α_{dl} values, exhibiting the most non-ideal capacitor behavior, probably due to the non-homogenous porous surface, responsible for the thin layer and convergent diffusion mechanisms [32].

Among the investigated electrodes, the PCA-RGO/Au NPs modified C-SPEs have the lowest R_{ct} , according to the observed highest electroactivity of such electrodes (Figure 2). On the other hand, PCA-RGO has the highest R_{ct} , that of the Au NPs is quite low, and PCA-RGO@Au NPs has an intermediate R_{ct} , likely due to a merging of the properties of PCA-RGO and Au NPs (Table 2).

In Figure 3B, the Bode plots of the hybrid electrodes have the maximum of the phase angle shifted to lower frequencies, meaning that the reaction is more energetically favored and the system less perturbed. As a matter of fact, in addition to the Randles circuit, another circuit has been added in the scheme of the equivalent circuit of hybrid electrodes. This likely originates from the interface region between the C-SPE and the electroactive material [36]. In this case, CPE_m and R_m are the capacitance and the resistance of the material, respectively.

Finally, the mass transfer resistance, expressed by the Warburg elements (Z_w , τ_w and α_w), is comparable for the PCA-RGO/Au NPs and the Au NPs modified electrodes and is 2-fold lower in PCA-RGO and PCA-RGO@Au NPs (Table 2). These values have resulted from the interplay between the massive transport of the probe, which is affected not only by its charge, but also by steric hindrance effects that contribute to increasing it. In the case of PCA-RGO, the massive transport could be favored by thin layer diffusion effects, absent in Au NPs [37], that are instead surface coordinated by the aromatic thiol that contributes, with its steric hindrance, to increasing the Z_w value.

3.3. Electroanalytical Applications of PCA-RGO/AuNPs Hybrid Nanocomposite

The electrodes modified by PCA-RGO/Au NPs have been tested for the electroanalytical detection of As(III) in water by anodic stripping voltammetry (ASV) by using a conventional three-electrode cell.

The stripping technique has relied first on a preconcentration step in which As_2O_3 is reduced to As(0), and then on a linear anodic scan for inducing reoxidation to As(III). The best accumulation potential in the cathodic region has been found -0.8 V (SCE); for lower potentials it is not possible to effectively accumulate As(III) at the electrode surface by reduction, because of the concomitant evolution of hydrogen at the electrodes.

Figure 4 reports the ASV scans collected at the PCA-RGO/Au NPs, Au NPs, PCA-RGO, and PCA-RGO@Au NPs electrodes from a 10^{-5} M As_2O_3 aqueous solution, for an accumulation time of 60 s and voltage of -0.8 V (SCE).

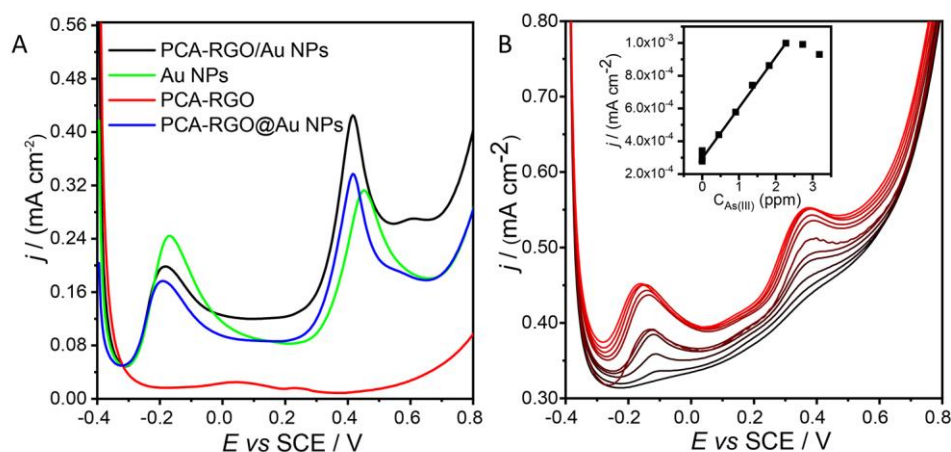


Figure 4. (A) ASV curves at the PCA–RGO/Au NPs, PCA–RGO, Au NPs, PCA–RGO@Au NPs electrodes in 10^{-5} M As_2O_3 in 0.1 M PBS solution at pH 7.4. (B) ASV curves after consecutive additions of As_2O_3 in solution, in the concentration range of 10^{-4} – 10^{-7} M, and (inset) corresponding calibration curve obtained from the density current values of the peak at +0.4 V (SCE).

No oxidation currents have been observed at the PCA-RGO electrode. Thus, this electrode is not electroactive in the As(0) oxidation, underscoring the fundamental role of Au NPs in inducing such a process. In addition, the ASV scans have shown two distinct peaks of oxidation at ca. -0.2 V (SCE) and $+0.4$ V (SCE), respectively (Figure 4A).

In order to explain and assign the oxidation peaks observed in Figure 4, anodic scans in the voltage ranges from -0.4 V (SCE) to $+0.1$ V (SCE) and from $+0.1$ V (SCE) to $+0.8$ V (SCE) have been collected in As_2O_3 aqueous solutions, with and without the accumulation step at -0.8 V (SCE) (data not shown). The results have shown that, when the accumulation step is not performed, the first signal at ca. -0.2 V (SCE) is not detected, while the second signal at ca. $+0.4$ V (SCE) is present. Moreover, when aliquots of the As_2O_3 solution have been subsequently added and ASV scans recorded, only the oxidation peak at $+0.4$ V (SCE) is observed and, as expected, it has been found to increase (data not shown).

Such results have suggested that the first peak is due to the oxidation of As(0) to As(III) and the second signal is related to the consecutive oxidation of As(III) to As(V). In fact, if the accumulation step is not performed at the beginning of the analysis, As(III) is not reduced, and its oxidation peak is not detected in the following anodic scan.

Figure 4A shows that the PCA-RGO/Au NPs electrodes have the same intensity of anodic peaks, at -0.2 V, as the Au NPs electrodes. Owing to the fact that, as demonstrated by Figure 4A, only the Au NPs catalyze the oxidation of As(0) and PCA-RGO are not electroactive, the evidence that the PCA-RGO/Au NPs electrodes provide the same answer as the Au NPs with a lower concentration of NPs, underlines, once again, the beneficial effects of the PCA-induced NPs-RGO electron coupling, contributing to enhancing faradaic current.

The sensitivity of the modified electrodes toward As(III) detection has been investigated, and the LODs in the concentration range of 10^{-7} M to 10^{-4} M have been estimated. Calibration curves have been recorded for the C-SPEs modified with PCA-RGO/Au NPs, Au NPs and PCA-RGO@Au NPs (data not shown).

Figure 4B reports the ASV scans of the PCA-RGO/Au NPs electrodes after subsequent additions of As_2O_3 in solution. The inset shows the calibration curve obtained with the results at the second oxidation peak, namely at $+0.4$ V (SCE)).

The sensitivity (*S*), detection limit (LOD) and quantification limit (LOQ) values of the investigated electrodes are reported in Table 3.

Table 3. Sensitivity (*S*), Detection limit (LOD) and quantification limit (LOQ) estimated for the PCA-RGO/Au NPs, PCA-RGO, Au NPs, and PCA-RGO@Au NP-modified C-SPEs in the detection of As(III) in PBS 0.1 M at pH 7.4. LOD and LOQ are calculated as $(3.29 s_b/S)$ and $(10 s_b/S)$, respectively.

Electrode	<i>E</i> = −0.2 (SCE)				<i>E</i> = +0.4 (SCE)			
	<i>S</i> / (A cm ^{−2} ppm ^{−1})	R ²	LOD/ ppb	LOQ/ Ppb	<i>S</i> / (A cm ^{−2} ppm ^{−1})	R ²	LOD/ ppb	LOQ/ ppb
PCA-RGO/Au NPs	1.8×10^{-2}	0.98	26	80	1.4×10^{-2}	0.98	19	58
Au NPs	3.5×10^{-3}	0.99	25	76	7.7×10^{-3}	0.95	22	67
PCA-RGO@Au NPs	5.2×10^{-4}	0.97	270	820	1.1×10^{-3}	0.96	480	1500

Table 3 shows that the Au NPs and PCA-RGO/Au NPs have comparable LODs and LOQs, but the sensitivity is significantly higher in the latter, confirming the highest electroactivity of the hybrid electrodes. On the other hand, the PCA-RGO@Au NPs sample shows much lower sensitivities and much higher LODs and LOQs than even the sample of neat Au NPs.

The LODs and LOQs estimated for the hybrid electrodes have been found extremely promising, since they are of the same order of magnitude of the limits imposed by the directives and laws on the maximum amount of As in public water supplies (i.e., 10 ppb as established by U.S. EPA) and also in line with the values reported for other electrochemical sensors based on Au-graphene hybrids [16,18–20] (Table S1 of Supporting Information).

4. Conclusions

A novel hybrid nanocomposite based on 1-pyrene-carboxylic acid (PCA)-modified RGO flakes, surface decorated with 3,4-dimethylbenzenethiol (DMBT)-capped Au NPs, 2–3 nm in size, has been synthesized, comprehensively characterized, and tested for the voltammetric detection of As (III) in aqueous solutions.

The comparison of the electrochemical and electrical properties of the hybrid nanocomposite with those of its single components and of the layer-by-layer junction after deposition onto C-SPEs, by CV and EIS, has demonstrated the higher electroactivity of the hybrid C-SPEs, which has been accounted for by (i) the hot spot electroactive behaviors of the Au NPs anchored onto the PCA-RGO platform, which form a microarray of electrodes, and hence, are responsible for the occurrence of convergent diffusion mechanisms, and (ii) the NPs-RGO electron coupling, provided by the PCA molecules anchored onto the RGO basal plane by π - π interactions, responsible for an increase of the electrode conductivity and of heterogeneous charge transfers at the electrode/electrolyte interphase—as well as for thin layer effects at the electrode surface.

The achieved hybrid modified C-SPEs have demonstrated to be highly effective in the detection of As(III), one of the most toxic and dangerous pollutants in water. The estimated LODs and LOQs are in line with the values reported in the literature and are of the same order of magnitude of the LODs imposed by the directives and laws of the U.S. EPA.

Supplementary Materials: The following supporting information can be downloaded at: <https://www.mdpi.com/article/10.3390/chemosensors10020067/s1>, Table S1: Examples of LODs and dynamic ranges of some nanocomposite-modified electrodes for As(III) determination.

Author Contributions: C.I. and M.L.C. contributed to the synthesis of the nanocomposite material and the writing of the manuscript. V.P., A.T. and L.F. carried out the electrochemical and electrical characterization of the material, as well as the sensing tests. I.P. contributed to writing and project management. All of the authors carried out the discussion and interpretation of data and contributed to writing the manuscript. All authors have read and agreed to the published version of the manuscript.

Funding: This research was funded by National Project PRIN 2012 prot. 20128ZZS2H, CNR-MHESR bilateral project “Analytical Toolkit for Monitoring Water Pollution”, PON project Research and

Innovation (2014–2020) TARANTO_ARS01_00637. PON project Research and Innovation (2014–2020) ECOTEC _ARS 01_00951.

Informed Consent Statement: Not applicable.

Conflicts of Interest: The authors declare no conflict of interest. The funders had no role in the design of the study; in the collection, analyses, or interpretation of data; in the writing of the manuscript, or in the decision to publish the results.

References

1. Ingrosso, C.; Petrella, A.; Curri, M.L.; Striccoli, M.; Cosma, P.; Cozzoli, P.D.; Agostiano, A. Photoelectrochemical properties of Zn(II) phthalocyanine/ZnO nanocrystals heterojunctions: Nanocrystal surface chemistry effect. *Appl. Surf. Sci.* **2005**, *246*, 367–371. [[CrossRef](#)]
2. Kumunda, C.; Adekunle, A.S.; Mamba, B.B.; Hlongwa, N.W.; Nkambule, T.T.I. Electrochemical Detection of Environmental Pollutants Based on Graphene Derivatives: A Review. *Front. Mater.* **2021**, *7*, 616787. [[CrossRef](#)]
3. Mondal, A.; Prabhakaran, A.; Gupta, S.; Subramanian, V.R. Boosting Photocatalytic Activity Using Reduced Graphene Oxide (RGO)/Semiconductor Nanocomposites: Issues and Future Scope. *ACS Omega* **2021**, *6*, 8734–8743. [[CrossRef](#)] [[PubMed](#)]
4. Ingrosso, C.; Corricelli, M.; Disha, A.; Fanizza, E.; Bianco, G.V.; Depalo, N.; Panniello, A.; Agostiano, A.; Striccoli, M.; Curri, M.L. Solvent dispersible nanocomposite based on Reduced Graphene Oxide in situ decorated with gold nanoparticles. *Carbon* **2019**, *152*, 777–787. [[CrossRef](#)]
5. Wuana, R.A.; Okieimen, F.E. Heavy Metals in Contaminated Soils: A Review of Sources, Chemistry, Risks and Best Available Strategies for Remediation. *ISRN Ecol.* **2011**, *2011*, 402647. [[CrossRef](#)]
6. Susan, A.; Rajendran, K.; Sathyasivam, K.; Krishnan, U.M. An overview of plant-based interventions to ameliorate arsenic toxicity. *Biomed. Pharmacother.* **2019**, *109*, 838–852. [[CrossRef](#)] [[PubMed](#)]
7. Sun, J.; Zhang, X.; Zhang, A.; Liao, C. Preparation of Fe-co based MOF-74 and its effective adsorption of arsenic from aqueous solution. *J. Environ. Sci.* **2019**, *80*, 197–207. [[CrossRef](#)]
8. U.S. Environmental Protection Agency. *Analytical Methods Support Document for Arsenic in Drinking Water*. Available online: <https://nepis.epa.gov/Exe/ZyPDF.cgi?Dockey=2000JT4N.txt> (accessed on 19 December 2021).
9. Ghaedi, M.; Ahmadi, F.; Shokrollahi, A. Simultaneous Preconcentration and Determination of Copper, Nickel, Cobalt and Lead Ions Content by Flame Atomic Absorption Spectrometry. *J. Hazard. Mater.* **2007**, *142*, 272–278. [[CrossRef](#)]
10. Huang, C.; Hu, B. Silica-Coated Magnetic Nanoparticles Modified with γ -Mercaptopropyltrimethoxysilane for Fast and Selective Solid Phase Extraction of Trace Amounts of Cd, Cu, Hg, and Pb in Environmental and Biological Samples Prior to Their Determination by Inductively Coupled plasma mass spectrometry. *Spectrochim. Acta Part B At. Spectrosc.* **2008**, *63*, 437–444. [[CrossRef](#)]
11. Faraji, M.; Yamini, Y.; Saleh, A.; Rezaee, M.; Ghambarian, M.; Hassani, R. A Nanoparticle-Based Solid-Phase Extraction Procedure Followed by Flow Injection Inductively Coupled Plasma-Optical Emission Spectrometry to Determine Some Heavy Metal Ions in Water Samples. *Anal. Chim. Acta* **2010**, *659*, 172–177. [[CrossRef](#)]
12. Aragay, G.; Merkoçi, A. Nanomaterials Application in Electrochemical Detection of Heavy Metals. *Electrochim. Acta* **2012**, *84*, 49–61. [[CrossRef](#)]
13. Palchetti, I.; Upjohn, C.; Turner, A.P.F.; Mascini, M. Disposable screen-printed electrodes (SPE) mercury-free for the lead detection. *Anal. Lett.* **2000**, *33*, 1231–1246. [[CrossRef](#)]
14. Bansod, B.K.; Kumar, T.; Thakur, R.; Rana, S.; Singh, I. A Review on Various Electrochemical Techniques for Heavy Metal Ions Detection with Different Sensing Platforms. *Biosens. Bioelectron.* **2017**, *94*, 443–455. [[CrossRef](#)] [[PubMed](#)]
15. Thakkar, S.; Dumée, L.F.; Gupta, M.; Singha, B.R.; Yang, W. Nano-Enabled sensors for detection of arsenic in water. *Water Res.* **2021**, *188*, 116538–116550. [[CrossRef](#)] [[PubMed](#)]
16. Jijana, A.N.; Mphuthi, N.; Shumbula, P.; Vilakazi, S.; Sikhwivhilu, L. The Ultra-sensitive Electrochemical Detection of As(III) in Ground Water Using Disposable L-cysteine/Lipoic Acid Functionalised Gold Nanoparticle Modified Screen-Printed Electrodes. *Electrocatalysis* **2021**, *12*, 310–325. [[CrossRef](#)]
17. Morales-Narváez, E.; Baptista, P.; Luis, M.; Zamora, G.A.; Merkoçi, A. Graphene-based biosensors: Going simple. *Adv. Mater.* **2017**, *29*, 1604905–1604912. [[CrossRef](#)] [[PubMed](#)]
18. Subramanian, S.; Elaiyappillai, E.; Asir, O.; Arulappan, D.; Palanisamy, S.; Princy, M.J.; Subramanian, R.; Samuel, V.J. Electrochemical Detection of Trace Amounts of Arsenic (III) in Poultry Using a Graphene Oxide-Bis(2-(4,5-diphenyl-1Himidazol-2-yl)phenoxy)Cobalt Composite Modified Electrode. *Electron. Mater.* **2019**, *48*, 4498–4506. [[CrossRef](#)]
19. Srikant, S.; Kumar, S.P.; Kumar, S.A. Gold Nano Particle and Reduced Graphene Oxide. Composite Modified Carbon Paste Electrode for the Ultra Trace Detection of Arsenic (III). *Electroanalysis* **2017**, *29*, 1400–1409.
20. Zhang, X.; Zeng, T.; Hu, C.; Hu, S.; Tian, Q. Studies on fabrication and application of arsenic electrochemical sensors based on titanium dioxide nanoparticle modified gold strip electrodes. *Anal. Methods* **2016**, *8*, 1162–1169. [[CrossRef](#)]
21. Brust, M.; Walker, M.; Bethell, D.; Schiffrin, D.J.; Whyman, R.J. Synthesis of thiol-derivatised gold nanoparticles in a two-phase Liquid-Liquid system. *Chem. Soc. Chem. Commun.* **1994**, *7*, 801–802. [[CrossRef](#)]

22. Chua, C.K.; Pumera, M. Chemical reduction of graphene oxide: A synthetic chemistry viewpoint. *Chem. Soc. Rev.* **2014**, *43*, 291–312. [[CrossRef](#)] [[PubMed](#)]
23. Ferrari, A.C.; Robertson, J. Interpretation of Raman spectra of disordered and amorphous carbon. *Phys. Rev. B* **2000**, *61*, 14095–14107. [[CrossRef](#)]
24. Li, L.; Zheng, X.; Wang, J.; Sun, Q.; Xu, Q. Solvent-Exfoliated and Functionalized Graphene with Assistance of Supercritical Carbon Dioxide. *ACS Sustain. Chem. Eng.* **2013**, *1*, 144–151. [[CrossRef](#)]
25. Zhuo, Q.; Ma, Y.; Gao, J.; Zhang, P.; Xia, Y.; Tian, Y.; Sun, X.; Zhong, J.; Sun, X. Facile synthesis of graphene/metal nanoparticle composites via self-catalysis reduction at room temperature. *Inorg. Chem.* **2013**, *52*, 3141–3147. [[CrossRef](#)] [[PubMed](#)]
26. Ghosh S., K.; Nath, S.; Kundu, S.; Esumi, K.; Pal, T. Solvent and Ligand Effects on the Localized Surface Plasmon Resonance (LSPR) of Gold Colloids. *J. Phys. Chem. B* **2004**, *108*, 13963–13971. [[CrossRef](#)]
27. Ingrosso, C.; Corricelli, M.; Bettazzi, F.; Konstantinidou, E.; Bianco, G.V.; Depalo, N.; Striccoli, M.; Agostiano, A.; Curri, M.L.; Palchetti, I. Au nanoparticle in situ decorated RGO nanocomposites for highly sensitive electrochemical genosensors. *J. Mater. Chem. B* **2019**, *7*, 768–777. [[CrossRef](#)]
28. Ambrosi, A.; Pumera, M. Electrochemistry at CVD Grown Multilayer Graphene Transferred onto Flexible Substrates. *J. Phys. Chem. C* **2013**, *117*, 2053–2058. [[CrossRef](#)]
29. Liu, L.; Ryu, S.; Tomasik, M.R.; Stolyarova, E.; Jung, N.; Hybertsen, M.S.; Steigerwald, M.L.; Brus, L.E.; Flynn, G.W. Seed/catalyst-free growth of zinc oxide nanostructures on multilayer graphene by thermal evaporation. *Nano Lett.* **2008**, *8*, 1965–1970. [[CrossRef](#)]
30. Bettazzi, F.; Ingrosso, C.; Pifferi, V.; Falciola, L.; Curri, M.L.; Palchetti, I. Gold Nano-particles Modified Graphene Platforms for Highly Sensitive Electrochemical Detection of Vitamin C in infant Food and Formulae. *Food Chem.* **2021**, *334*, 128692–128700. [[CrossRef](#)]
31. Cumba, L.R.; Foster, C.W.; Brownson, D.A.C.; Smith, J.P.; Iniesta, J.; Thakur, B.; do Carmo, D.R.; Banks, C.E. Can the mechanical activation (polishing) of screen-printed electrodes enhance their electroanalytical response? *Analyst* **2016**, *141*, 2791–2799. [[CrossRef](#)]
32. Compton, R.G.; Banks, C.E. *Understanding Voltammetry*; Imperial College Press: London, UK, 2011.
33. Brownson, D.A.C.; Kampouris, D.K.; Banks, C.E. Graphene electrochemistry: Fundamental concepts through to prominent applications. *Chem. Soc. Rev.* **2012**, *41*, 6944–6976. [[CrossRef](#)] [[PubMed](#)]
34. Liu, X.; Cong, R.; Cao, L.; Liu, S.; Cui, H. The structure, morphology and photocatalytic activity of graphene–TiO₂ multilayer films and charge transfer at the interface. *New J. Chem.* **2014**, *38*, 2362–2367. [[CrossRef](#)]
35. Vasudevan, S.; Lakshmi, J. The Adsorption of Phosphate by Graphene from Aqueous Solution. *RSC Adv.* **2012**, *2*, 5234–5242. [[CrossRef](#)]
36. Lo Presti, L.; Pifferi, V.; Di Liberto, G.; Cerrato, G.; Ceotto, M. Direct measurement and modeling of spontaneous charge migration across anatase-brookite nanoheterojunctions. *J. Mater. Chem. A* **2021**, *9*, 7782–7790. [[CrossRef](#)]
37. Orazem, M.E.; Tribollet, B. *Electrochemical Impedance Spectroscopy*; John Wiley & Sons: New York, NY, USA, 2008.